Polarized plasmonic enhancement by Au nano structures probed through Raman scattering of suspended graphene

Sebastian Heeg,[*,†] Roberto Fernandez-Garcia,[‡] Antonios Oikonomou,[¶] Fred Schedin,[§] Rohit Narula,[†] Stefan A. Maier,[‡] Aravind Vijayaraghavan,[¶,§] and Stephanie Reich[†]

Department of Physics, Freie Universität Berlin, 14195 Berlin, Germany, Department of Physics, Imperial College London, London SW7 2AZ, UK, School of Computer Science, The University of Manchester, Manchester M13 9PL, UK, and Centre for Mesoscience and Nanotechnology, The University of Manchester, Manchester M13 9PL, UK

E-mail: sebastian.heeg@physik.fu-berlin.de

Abstract

We characterize plasmonic enhancement in a hotspot between two Au nano disks using Raman scattering of graphene. Single layer graphene is suspended across the dimer cavity and provides an ideal two-dimensional test material for the local near field distribution. We detect a Raman enhancement of the order of 10^3 originating from the cavity. Spatially resolved Raman measurements reveal a near field localization one order of magnitude smaller than the wavelength of the excitation, which can be turned off by rotating the polarization of the excitation.

[*]To whom correspondence should be addressed
[†]Department of Physics, Freie Universität Berlin, 14195 Berlin, Germany
[‡]Department of Physics, Imperial College London, London SW7 2AZ, UK
[¶]School of Computer Science, The University of Manchester, Manchester M13 9PL, UK
[§]Centre for Mesoscience and Nanotechnology, The University of Manchester, Manchester M13 9PL, UK

The suspended graphene is under tensile strain. The resulting phonon mode softening allows for a clear identification of the enhanced signal compared to unperturbed graphene.

Keywords: Raman spectroscopy, enhancement, plasmonic cavity, suspended graphene, strain

For its fundamental physics and technological applications, graphene has attracted enormous interest since its experimental discovery.[1] It has become the model system for two-dimensional materials, and its ballistic conduction at room temperature[2] makes graphene a promising material for transistors, interconnects and a variety of optoelectronic applications.[1–3] Recently, the combination of graphene with plasmonic nano structures has substantially improved the photo detection capabilities of graphene.[4–6]

From a spectroscopic point of view, surface enhanced Raman scattering (SERS) has become a spectacular application of plasmonics.[7] It combines the generation of highly localized light fields at metal-dielectric interfaces with the variety of properties that can be obtained by Raman spectroscopy, such as strain,[8] doping[9] or the nature of defects[10] in the case of graphene. The 2D nature of graphene and its well known Raman spectrum makes it a favorable test bed for investigating the mechanisms of SERS. A variety of nano particle geometries has proven to deliver considerable Raman enhancement factors, such as well defined arrays of gold nano disks on top of a graphene/SiO_2 system,[11] densely packed gold-nanopyramids[12] and a photonics crystal nano cavity[13] covered with graphene. An alternative way to control the generation of highly enhanced electromagnetic fields is to create a nanoscale cavity formed by closely placed metallic nanoparticles of defined geometry, allowing for instance single-molecule detection.[14]

In this paper we demonstrate a graphene Raman enhancement up to 10^3 arising from a nanoscale cavity between two closely spaced gold nanodisks. Graphene is suspended between the two disks and partially extends into the cavity. Spatially resolved Raman measurements reveal that the enhancement in the cavity is localized in an area one order of magnitude smaller than the wavelength of the excitation. Upon rotating the polarization, we decouple the two disks, which now act as two separated plasmonic particles. The enhancement factor drops by a factor of 20 and the localization

is lifted. The enhanced Raman signal exclusively arises from suspended graphene under tensile strain, which is induced by the double structure partially elevating the graphene. This allows us to simultaneously probe strained and unstrained graphene. Raman enhancement in strained graphene can be used to characterize plasmonic enhancement arising from any variety of nano-structure geometries. We demonstrate the method and analysis on a double-dot structure, which can be applied to any other desired plasmonic structure.

A SEM picture of the double structure we investigate is shown in the inset of Figure 1(a). It consists of two disks with a height of 45 nm (5 nm Cr + 40 nm Au), and diameter of $\sim$ 100 nm with an inter particle distance of $\sim$ 30 nm on a flat SiO_2 surface of 300 nm thickness. Graphene is prepared by mechanical cleavage and transferred on top of the structures. Atomic force microscope measurements reveal the topography of the graphene layer deposited on top of the double dot structure as shown in Figure 1(a). The graphene layer is suspended over the gap between the two particles and between the edge of the particles and the surrounding substrate over a length of around 150 nm in all directions. The colored arrows indicate height profiles at different topographic conditions shown in Figure 1(b), such as crossing the particle centers and the gap (red), and crossing the edge of the particles and the gap (blue). The green arrow shows the graphene suspended at half the height of the antennas and the black arrow indicates graphene completely adsorbed on the substrate. Figure 1(c) shows a sketch of the sample configuration.

The observed topography suggests that the graphene is under tensile strain, which is defined by the corresponding relative elongation $\Delta L/L_0$ as $\varepsilon_x = \Delta L_x/L_x$ and $\varepsilon_y = \Delta L_y/L_y$ within our laboratory frame. The strain configuration $(\varepsilon_x, \varepsilon_y)$ varies for different locations on and around the structure. We expect the strain components to be maximal on top of and in the very vicinity of the structures, decreasing outwards. As we will show in the course of the data analysis, Raman spectroscopy limits the sum of ε_x and ε_y to $< 1\%$.

In comparison to a perfect graphene sheet of equal lateral dimensions, the height profiles crossing the particle centers yield maximal relative elongations/strains of $\varepsilon_x, \varepsilon_y > 2.5\%$, assuming zero elongation at the unsuspended parts. These values are about five times higher than the values de-

duced from Raman spectroscopy and seem to be unrealistically high; calculations on pressurized graphene balloons state that strains of 5% require adhesion energies of $3\,\mathrm{J/m^2}$,[15] which is roughly ten times the experimentally obtained values of $0.45\,\mathrm{J/m^2}$ on SiO_2.[16] For strains derived from the topology only, one would therefore expect immediate delamination, resulting in an increase of the suspended parts and a reduction of the energy stored in strain.

The differences can be explained by two main mechanisms. Firstly, during processing and transfer the graphene/PMMA sandwich is placed on top of the structures and bends slightly, partially reflecting their topology. Therefore, the reference for the geometric calculations is larger than the assumed flat graphene sheet, which as a result reduces the relative elongation. Secondly, the graphene shows wrinkles and undulation on the suspended parts and on SiO_2, which lessens the relative elongation further. While the topology fails to quantitatively deliver the true strain, we observe a dominating strain in y-direction, as the graphene is pulled ca. 4 nm into the gap between the two particles. Optical images, and topographic data on this and additional structures are presented in the Supporting information.

Figure 1(d) shows the scattering cross section (dots) of the double structure obtained by polarized dark field spectroscopy before graphene deposition. The polarization P_X of the illumination source is oriented along the x-axis defined in (a). In order to obtain the maximum SERS enhancement, the plasmonic antennas were designed in such a way that the P_X resonance matches the excitation laser of 638 nm excitation. We simulate the scattering cross section of the double structure for P_X and P_Y, where P_Y is blue shifted compared to P_X, using a commercially available finite-difference-timedomain code (Lumerical FDTD). The polarization dependence of the simulated scattering cross section is explained by near field coupling. The localized plasmon resonance of a single metallic particle depends on its material, shape, and size. If the distance between two adjacent particle becomes small ($d \ll \lambda$), they interact via their near field. This interaction leads to (i) a shift in the scattering cross section compared to single particles and (ii) a strong near field localization in the cavity formed between the two particles. Using disks instead of rods as optical antennas allows us to quantify the coupling effect between the two particles by rotating the excita-

tion polarization. In our case, P_X couples the particles and P_Y lets them act as two single particles. Geometrical deviations of the real particles - such as non perfect edges - cause a blueshift of the experimental data compared to our simulation. In addition, the effect of the Cr adhesive layer may be underestimated in simulations and contribute to the blueshift.[17]

The wavelengths of the scattered light corresponding to the G and $2D$ peaks - the dominant phonons observed in graphene Raman spectra - are indicated in Figure 1(d) for the two laser lines employed. Especially the energy of the $2D$ phonon E_{ph} is of the same order of magnitude as the line width Γ of the plasmon. We are therefore able to distinguish rudimentarily between the regimes of enhanced absorption (red) and enhanced emission (green) and expect the SERS enhancement factor to scale with the square of the field enhancement factor $|E_{Loc}|/|E|$ for both cases. This can be clearly distinguished from scaling with the fourth power of field enhancement, which is generally observed in SERS for $E_{ph} \ll \Gamma$.[18,19]

Figure 2 shows the Raman spectra taken on the structures for 532 nm (green, (a) and (b)) and 638 nm excitation (red, (c) and (d)) for P_X ((a) and (c)) and P_Y ((b) and (d)). In all Raman measurements the analyzer in the spectrometer is set parallel to the polarization of the excitation. For comparison the spectrum of graphene on SiO_2 (black) under the same experimental conditions but 1.5 μm away from the structure is shown. All spectra are normalized to the $2D$ peak height on SiO_2. The position and the full width at half maximum (FWHM) of the G-peak ($\sim 1580/11\,\mathrm{cm}^{-1}$) and the $2D$ peak ($\sim 2670/25\,\mathrm{cm}^{-1}$) on SiO_2, extracted from Figure 2(a), confirm the presence of single layer graphene.[9] This is supported by the peak height ratio $2D/G$ of 2.8, which is in agreement with single-layer graphene for an excitation of 532 nm and an oxide layer thickness of 300 nm.[20,21] We relate the intensity drop on top of the dimer to the partial reduction of constructive interference (see Supporting information). Note that we concentrate on the $2D$ peak when evaluating the enhancement, as the G peak is not suitable for two reasons: the gold nano structures exhibit a luminescence,[22] whose shoulder overlaps with the G-peak (negligibly with $2D$) and generally cause noisier spectra. In addition, we observe peaks at $1450\,\mathrm{cm}^{-1}$ and $1530\,\mathrm{cm}^{-1}$ on top of the structure and next to it for 638 nm excitation, which we assign to remainders of the glue used in

graphene exfoliation.

Neglecting the shape and the position of the peaks observed on the structure at this stage, we find a good qualitative agreement between the observed signal intensities and scattering cross sections in Figure 1(d) with respect to enhanced absorption. The highest 2*D* intensity occurs for 638 nm and P_X, where the excitation is closest to the experimentally observed scattering cross section. Combining the lower simulated scattering cross section with the blueshift for P_Y - shifting the maximum further away from the excitation of 638 nm - leads to the enhancement we observe for P_Y. It is present, but less pronounced than for P_X.

Interestingly, we do not observe a notable enhancement for 532 nm with either polarization; while the scattered light is off the plasmon resonance for 638 nm, it is in resonance for 532 nm, yet no enhancement occurs. While this observation is not decisive regarding the conclusions of this work, the apparent lack of enhanced emission is certainly of interest regarding the mechanism of cavity induced SERS of graphene and is currently being studied. In the following, the term enhancement refers to enhanced absorption only.

In Figure 2(a) the 2*D* peak observed on top of the structures shifts down $9\,\mathrm{cm}^{-1}$ to $2661\,\mathrm{cm}^{-1}$ compared to the spectrum on SiO_2. Its width increases from $26\,\mathrm{cm}^{-1}$ to $37\,\mathrm{cm}^{-1}$. While we do not observe a downshift of the *G* peak within the resolution of our spectrometer, the FWHM increases from $11\,\mathrm{cm}^{-1}$ on SiO_2 to $17\,\mathrm{cm}^{-1}$ on the structure. Strain modifies crystal phonons; tensile strain results in a phonon mode softening. We expect a frequency downshift from the graphene topology discussed earlier. In general, the 2*D* peak is more sensitive to strain than the *G*-peak,[8,23,24] which explains that we do not observe a downshift of the *G*-peak in the presence of peak broadening. The broadening itself reflects the spatial variations of the strain configurations on and around the structure. A similar behavior of the 2*D* peak has been observed by *Tomori et al.*,[25] when they deposited graphene on pillars made of e-beam resist and arrived at a comparable type of topography. The broadened *G*- and 2*D*-peaks and the downshifted 2*D*-peak on the structures represents the sum of all location in the laser focus.

Peak positions and widths change drastically when plasmonic enhancement comes into play.

In Figure 2(c), the $2D$ peak consist of three components; the two lower components arise from local hot spots where the enhanced near field from the particles interacts with strained graphene. The same mechanism applies to the now dominating G-peak component at $1558\,\mathrm{cm}^{-1}$. The uppermost $2D$- and G-components approximately match the peaks measured on SiO_2 in intensity and frequency. They stem from scattering in the laser focus which is not subject to plasmonic enhancement.

To evaluate the strain, we use the G mode and the $2D'$ mode ($3200\,\mathrm{cm}^{-1}$). The frequency of these Raman lines under strain depends only on changes in the force constants and is independent of the electronic structure.[26] For both the G and the D' modes, the change in frequency under strain $\Delta\omega^{\pm}_{E_{2G}}$ is given by[23,27,28]

$$\begin{aligned}\Delta\omega^{\pm}_{E_{2G}} &= \Delta\omega^{h}_{E_{2G}} \pm \frac{1}{2}\Delta\omega^{S}_{E_{2G}} \\ &= -\omega^{0}_{E_{2G}}\gamma_{E_{2G}}\varepsilon_h \pm \frac{1}{2}\omega^{0}_{E_{2G}}\beta_{E_{2G}}\varepsilon_s, \end{aligned} \quad (1)$$

where E_{2G} denotes the phonon symmetry, $\Delta\omega^{h}_{E_{2G}}$ is the shift due to the hydrostatic component of the strain $\varepsilon_h = \varepsilon_y + \varepsilon_x$ and $\Delta\omega^{S}_{E_{2G}}$ is the phonon splitting due to the shear component of strain $\varepsilon_s = \varepsilon_y - \varepsilon_x$[29] . The peak position at zero strain is given by $\omega^{0}_{E_{2G}}$, while $\gamma_{E_{2G}}$ denotes the Grüneisen parameter and $\beta_{E_{2G}}$ denotes the shear deformation potential of the corresponding vibration. Averaged spectra from a line scan (step size 100 nm) are shown for the G and $2D'$ mode in Figure 3(a) and (b), respectively. The G-mode shifts down $23\,\mathrm{cm}^{-1}$ and its FWHM increases from $17\,\mathrm{cm}^{-1}$[30] to $23\,\mathrm{cm}^{-1}$. For $2D'$, we observe a downshift of $44\,\mathrm{cm}^{-1}$ and an increase in the FWHM from $15\,\mathrm{cm}^{-1}$ to $20\,\mathrm{cm}^{-1}$. Neglecting the shear strain component, we insert the Grüneisen parameters $\gamma_G = 1.8$ and $\gamma_{2D'} = 1.6$[31] in Eq. (1) and obtain an excellent agreement between the hydrostatic strain components $\varepsilon_y + \varepsilon_x$ derived from G (0.82%) and $2D'$(0.81%). The broadening of the modes under strain indicates a non-vanishing shear strain. This is supported by the splitting of the $2D$-mode and the presumably dominant y-strain determined from the topology. For uniaxialy strained graphene, a G-peak splitting is recognizable at shear strains $> 0.4\%$.[23]We conclude that in the ar-

eas of plasmonic enhancement the graphene is under strain with a hydrostatic component $\approx 0.8\%$ and shear component $< 0.4\%$.

The $2D$-mode cannot be used for strain evaluation because of the non-standard strain configuration (i.e. graphene bending on a nm scale at the particle edges). In addition, the nature of the $2D$-peak splitting in the presence of shear strain is currently under debate in the literature.[24,32–34] While the overall intensity is assumed to be independent of polarization, the relative intensities and shift rates for each subpeak depend on the polarization of each excitation and emission, the orientation of the strain, the crystallographic axis and their combined relative orientations. Therefore we use the $2D$-peak only for evaluating the plasmonic enhancement via its intensity. Peak fits for P_X are provided in the supporting information. For polarization in y-direction, a comparable strain analysis is impossible, as the low signal intensities hamper the clear identification of a shifted G and $2D'$ mode.

By investigating the signal intensities and the strain configuration we have so far established that (i) the enhanced Raman peaks arise from areas under strain, indicating that (ii) the enhancement is localized around the particles and that (iii) the enhancement depends on the polarization. In the following, we show how the polarization dependence can be directly related to near field coupling for P_X - and the corresponding strong localization in the cavity - and the lack thereof for P_Y. In Figure 4(a) we depict a Raman line scan over the structure for 638 nm excitation and P_X, taken in x-direction with a step size of 100 nm. The spatial position of the laser focus relative to the antenna center is plotted versus the sum of integrated intensity of the three $2D$ components. The intensity is normalized to the integrated $2D$ intensity on SiO_2 away from the structure. As expected, the signal enhancement is maximal when the laser focus is centered on the structure. The profile represents the convolution of the laser spot, which has a FWHM of ≈ 570 nm, and the sites of localized enhancement. Raw data of the line scan and laser spot size are given in the Supporting information. A Gaussian fit delivers an enhancement factor of 12.8 with a FWHM of 610 nm for P_X, exceeding the FWHM of the laser spot by less than 10%. Figure 5(a) depicts the corresponding simulated near field enhancement $|E/E_0|^2$ at a height of 40 nm. Due to the near

field coupling of the particles, the enhancement is concentrated in the area between the particles and acts approximately like a point-like source.

Why do we choose to evaluate the near field at a height of 40 nm instead of the 45 nm, the nominal height of the particles? A near field cross section in the (x,z) plane is shown in Figure 5(b). The hot spots on the particles edges are caused by the lightning rod effect, which describes field enhancement as a purely geometrical phenomenon of electromagnetic field line crowding at sharp edges. While the assumption of perfect edges does not hold for real structures, the evaluation of the enhancement in the cavity is a very valid approximation. The height profiles shown in Figure 1(b) confirm that the graphene is suspended at a height of 41 nm in the gap center. Over the range of gap in the y-direction, the height drops to about 37 nm (see blue profile). Therefore we achieve the best correspondence between the simulation and experiment by examining the near field at a height of 40 nm instead of 45 nm. A spatial profile of the near field enhancement at $z = 40$ nm and $y = 0$ is given in Figure 5(c), where the cavity is indicated by the grey square.

In Figure 4(b) we depict a comparable Raman line scan for P_Y. A Gaussian fit yields a maximal enhancement factor of 3.2 and a FWHM of 840 nm. Here, the particles approximately act as two isolated particles. The near field - shown in Figure 5(d) - extends predominantly in y direction for each of the particles and no cavity enhancement is present. Scanning in x-direction, the simulation predicts two spatially separated scattering centers, which lead to the observed broadening of the intensity profile. As explained in the previous paragraph, we evaluate the near field at a height of 40 nm to avoid edge effects. A potential contribution of the particle top surface to the enhancement is negligible, as it does not depend on the polarization. If significant, it would smear the difference in the width of the intensity profiles of P_X and P_Y. To verify the correlation between polarization and near field coupling, we conduct similar line scans for 532 nm excitation and both polarizations. While we do not observe a notable enhancement, the effects of the structure can be transformed into a spatial profile which yields a width of around 710 nm for both polarizations (see Supporting information).

As the field is localized in a very small area compared to the laser spot, the actual enhancement

is significantly higher than the observed factor of 12.8 for P_X. In Figure 5(a), the dashed line encircles the area relevant for the enhancement. It includes 90% of the calculated integrated near field intensity within the cavity. Comparing this area with the size of the laser spot yields an overall enhancement of 4×10^3. Figure 6 shows how the enhancement depends on the near field intensity in the cavity considered to be relevant. Applying a similar analysis for P_Y yields an enhancement factor of 2.2×10^2. The area taken into account is indicated in Figure 5 (d) and (f). Again, the cut-off is set to 90% of the integrated near field intensity.

A comparison between the experimental enhancement factors for P_X and P_Y allows us to estimate the contribution from the outer particle edges to the cavity enhancement. Upon a 90° rotation, the near field at the outer particle edges for P_X approximately matches the near field for P_Y in shape and magnitude. This can be easily seen by comparing Figure 5(e) and (f). Therefore, 50% of experimentally observed enhanced intensity for P_Y represents the enhancement we expect from the outer particle edges for x-polarization. Inserting these values yields a contribution of around 12% - with each edge contributing 6% - and confirms that the observed enhancement predominantly arises from the cavity. This estimate appears reliable, as it is independent of the real near field distribution, factors in geometrical deviations of the particles compared to the simulation, and agrees well with localization observed in the intensity profile for P_X.

Note that the observed enhancement factor is inversely proportional to the estimated area of near field localization. As indicated in Figure 6, variations in the analytical approach may therefore leverage the same experimental data into enhancement factors that differ by orders of magnitude. For this reason it is difficult to relate our results to enhancement factors in the literature. In ref. 11, for instance, an experimental enhancement factor of 35 is observed for gold nano disks placed on top of graphene. The distance between the particles is too large to allow near field coupling but is too small to observe the signal from isolated particles. In addition, the authors chose not to factor in the area of near field localization, which would significantly increase the enhancement factor. *Wang et. al*[12] measure graphene placed on top of closely spaced gold nano pyramids, observing an enhancement factor of the order of 10^4 in the experiment; by assigning the enhancement to

a narrow area of $5 \times 5\,\mathrm{nm}$ - corresponding to a low percentage in Figure 6 - they arrive at an enhancement of 10^7. In addition, to our knowledge no surface enhanced Raman study on a single, isolated plasmonic dimer structure interfaced with graphene has been reported.

While we use the signal on SiO_2 as a reference, plasmonic enhancement occurs mainly at a height around $\sim 40\,\mathrm{nm}$. Therefore the interference effect due to the substrate has to be taken into account. Here, reflection and transmission at multiple interfaces (Si, SiO_2, graphene, air) of the excitation as well as the scattered light may lead to constructive or destructive interference, depending on the wavelength of excitation, emission and the oxide layer thickness.[20,21,35,36] Following the approach of Ref. 36, we arrive at a factor of 0.52 for 638 nm excitation on 300 nm SiO_2. An in depth-treatment of the interplay between interference and the cavity is beyond the scope of this work. In addition, it is doubtful that the picture of stratified media holds for the graphene topography in our sample configuration. We therefore neglect the interference effect for the suspended graphene and correct for the destructive interference on SiO_2, leading to an estimate of the enhancement $\geq 2 \times 10^3$.

The graphene suspended around and between the double structure serves two distinct purposes. From a purely plasmonics point of view, the graphene is a Raman active, two-dimensional membrane that serves as a detection channel of the near field distribution. In the areas of enhancement, its Raman signals are shifted and therefore allow a clear assignment. From the perspective of Raman scattering on graphene, the double structures suspend the graphene, induce local strain and simultaneously provide the means of local detection. The induced strain represents a configuration of hydrostatic and shear strain ($\varepsilon_h > \varepsilon_s > 0$), which can neither be achieved by uniaxial strain ($\varepsilon_s > \varepsilon_h > 0$) nor biaxial strain ($\varepsilon_h > 0, \varepsilon_s = 0$).

In conclusion, we probe with surface enhanced Raman scattering the plasmonic properties of an isolated double disk nano structure interfaced with suspended graphene. By rotating the polarization of the excitation, we switch between the dots acting as single plasmonic particles and a coupling regime, realizing a plasmonic cavity. In the cavity, we observe a plasmonic enhancement of the order of 10^3, where graphene serves as a two-dimensional, Raman active integrator of the

local near field. The enhanced signal arises from an area one order of magnitude smaller than the wavelength of the excitation and probes suspended graphene under strain. The combination of phonon softening and local enhancement will allow to study the impact of high electric fields on the electrical transport in graphene. Our approach may allow the induction of different types of local strain configurations via the shape, size, number, and arrangement of plasmonic nano particles, and simultaneously provide the means to locally probe them by surface enhanced Raman scattering. This approach can be extended to using silver - the preferred material in plasmonic due to low losses and resonances towards lower wavelengths; *Reed et al*[37] recently demonstrated that single layer graphene placed on top silver nano structures passivates their surface and maintains their performance by preventing oxidation.

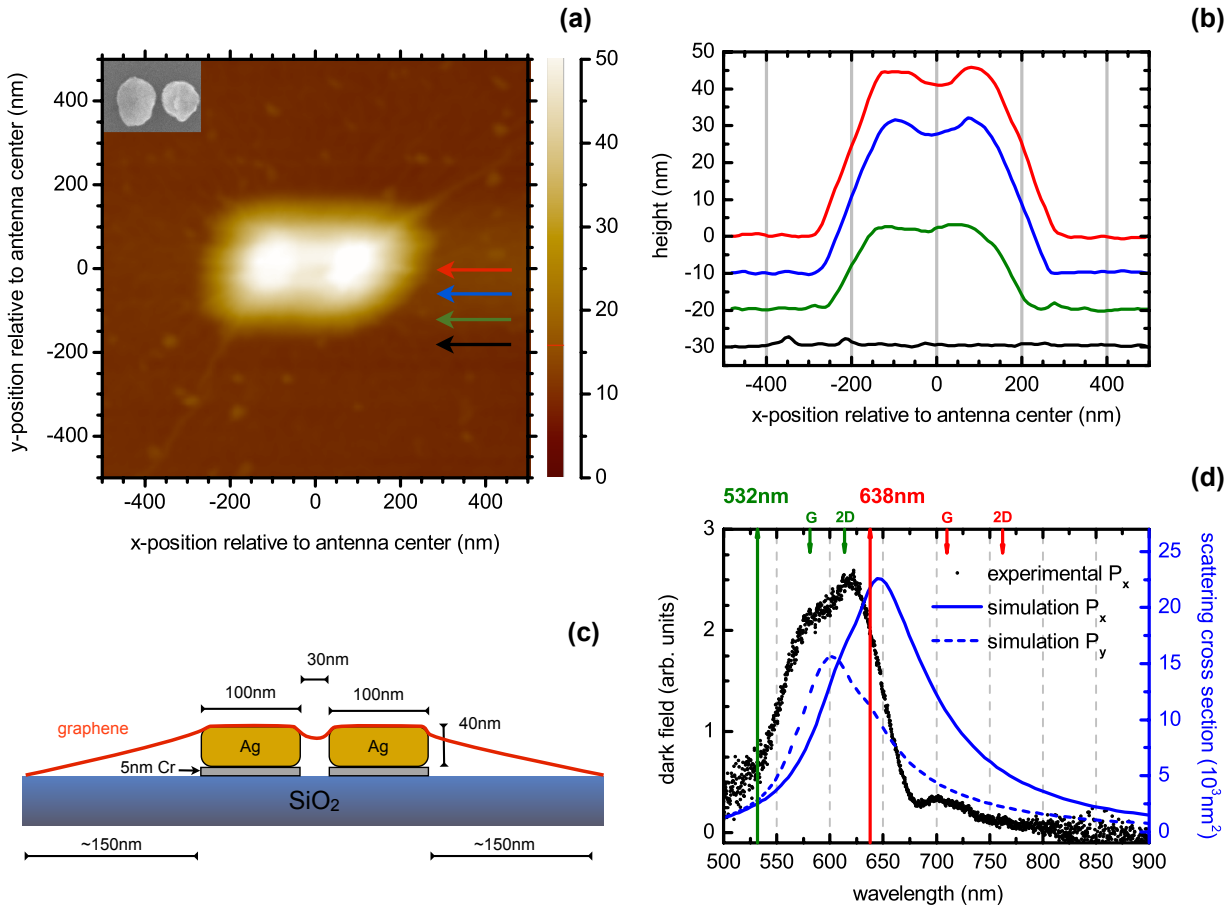

Figure 1: (a) AFM image of graphene placed on top of the double structure. The colored arrows indicate the y-position of the height profiles shown in (b). Each height profile is set off by 10 nm for clarity. (c) shows a sketch of the sample configuration. (d) depicts experimental dark field spectra (triangles) and simulated scattering cross sections for P_X (solid) and P_Y (dashed). The excitation wavelength employed in the Raman experiments are indicated as vertical lines, together with the corresponding wavelength of the *G* and 2*D* modes of graphene.

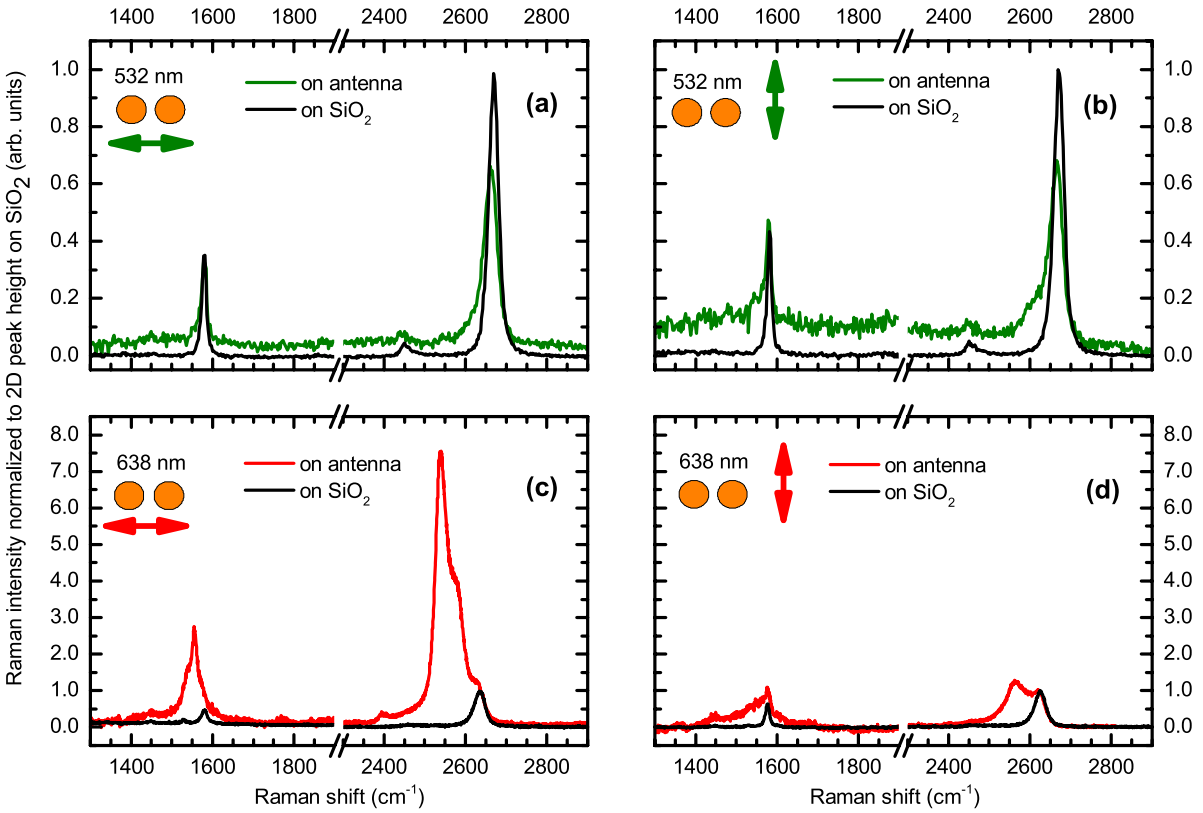

Figure 2: Raman spectra on the double structure for (a) $\lambda = 532\,\text{nm}$ and P_X, (b) $\lambda = 532\,\text{nm}$ and P_Y, (c) $\lambda = 638\,\text{nm}$ and P_X ,(d) $\lambda = 638\,\text{nm}$ and P_Y. The spectra are normalized to the $2D$ peak height measured on SiO_2 next to the structure for the corresponding excitation and polarization

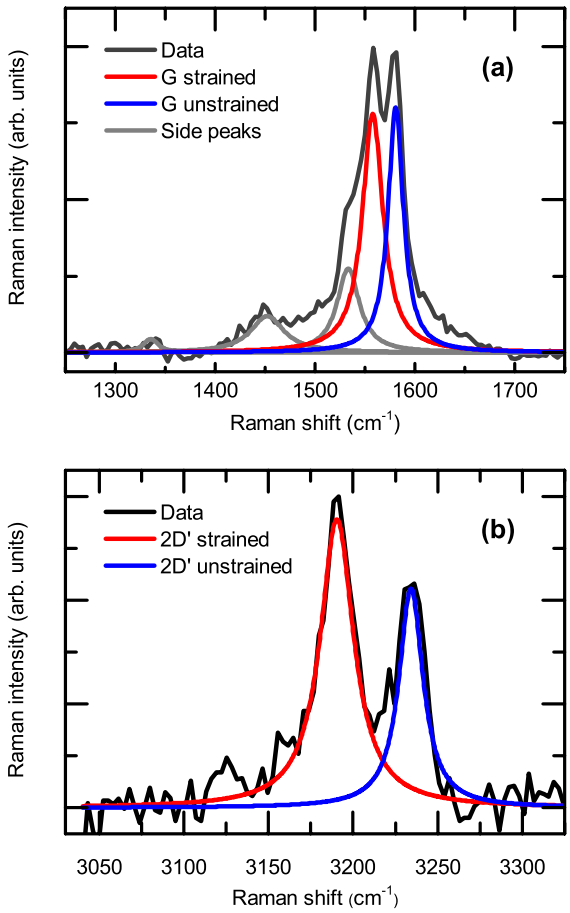

Figure 3: Sum of Raman spectra of (a) G mode and (b) $2D'$ mode obtained from a line scan over the structure with $\lambda = 638\,\mathrm{nm}$ and P_X. The peaks corresponding to strained graphene (red) are downshifted and compared to the peaks arising from unstrained graphene (blue).

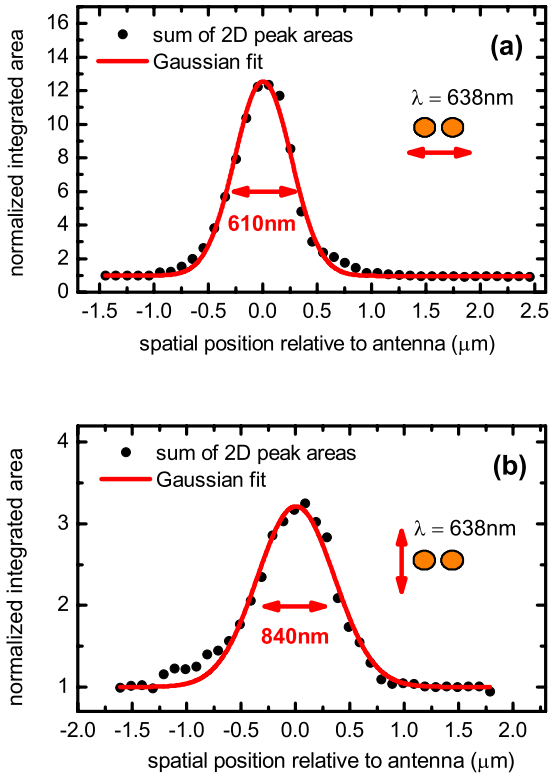

Figure 4: Raman line scan over the antenna structure, where the sum of all 2D peak components is plotted versus the spatial position of the laser focus for P_X(a) and P_Y(b) with $\lambda = 638\,\text{nm}$. The corresponding Gaussian fits including FWHM are shown.

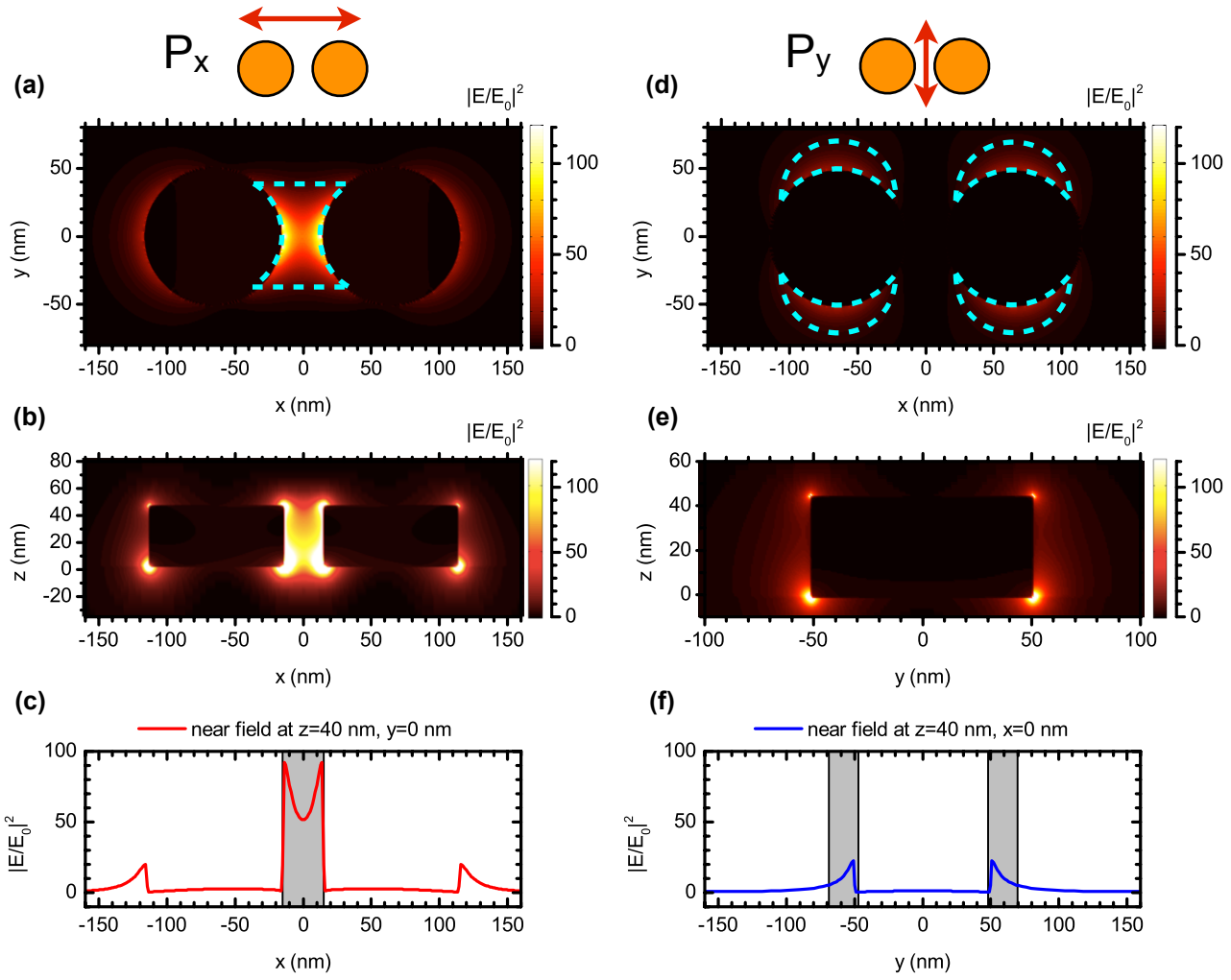

Figure 5: Near field enhancement $|E/E_0|^2$ for P_X is shown in the (x,y) plane at $z = 40\,\mathrm{nm}$ (a) and in the (x,z) plane at $y = 0$ (b). The area considered contributing to the enhancement is indicated in by the dashed line in (a). The corresponding data for P_Y is shown in (d) and (e). Cross sections of the near field enhancement relevant for the enhancement factor are given in (c) for P_X and (f) for P_Y.

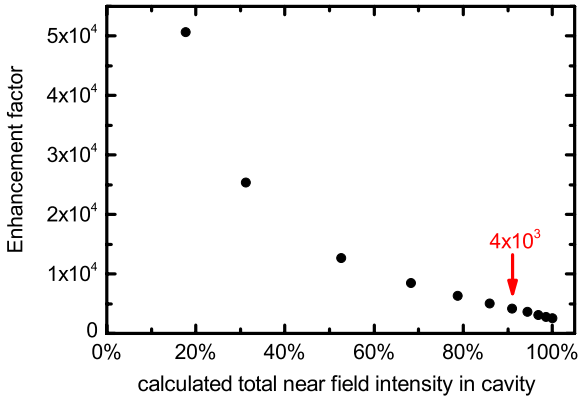

Figure 6: Percentage of total near field intensity in the cavity plotted versus the resulting enhancement factor. Taking into account 90% of the near field intensity yields an overall enhancement factor of ca. 4×10^3.

Table of contents graphic

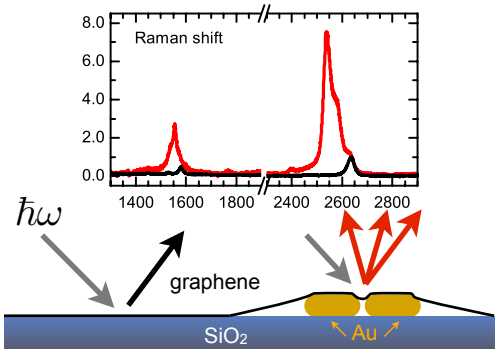

Notes and References

(1) Novoselov, K. S.; Geim, A. K.; Morozov, S. V.; Jiang, D.; Zhang, Y.; Dubonos, S. V.; Grigorieva, I. V.; Firsov, A. A. *Science* **2004**, *306*, 666–669.

(2) Geim, A. K.; Novoselov, K. S. *Nature Materials* **2007**, *6*, 183–191.

(3) Bonaccorso, F.; Sun, Z.; Hasan, T.; Ferrari, A. C. *Nature Photonics* **2010**, *4*, 611–622.

(4) Liu, Y.; Cheng, R.; Liao, L.; Zhou, H.; Bai, J.; Liu, G.; Liu, L.; Huang, Y.; Duan, X. *Nature Communications* **2011**, *2*, 579.

(5) Echtermeyer, T. J.; Britnell, L.; Jasnos, P. K.; Lombardo, A.; Gorbachev, R. V.; Grigorenko, A. N.; Geim, A. K.; Ferrari, A. C.; Novoselov, K. S. *Nature Communications* **2011**, *2*, 458.

(6) Fang, Z.; Liu, Z.; Wang, Y.; Ajayan, P. M.; Nordlander, P.; Halas, N. J. *Nano Lett.* **2012**, *12*, 3808–3813.

(7) Giannini, V.; Fernández-Domínguez, A. I.; Sonnefraud, Y.; Roschuk, T.; Fernández-García, R.; Maier, S. A. *Small* **2010**, *6*, 2498–2507.

(8) Huang, M.; Yan, H.; Chen, C.; Song, D.; Heinz, T. F.; Hone, J. *Proc. Natl. Acad. Sci. U.S.A.* **2009**, *106*, 7304–7308.

(9) Ferrari, A. C.; Meyer, J. C.; Scardaci, V.; Casiraghi, C.; Lazzeri, M.; Mauri, F.; Piscanec, S.; Jiang, D.; Novoselov, K. S.; Roth, S.; Geim, A. K. *Phys. Rev. Lett.* **2006**, *97*, 187401.

(10) Eckmann, A.; Felten, A.; Mishchenko, A.; Britnell, L.; Krupke, R.; Novoselov, K. S.; Casiraghi, C. *Nano Lett.* **2012**, *12*, 3925–3930.

(11) Schedin, F.; Lidorikis, E.; Lombardo, A.; Kravets, V. G.; Geim, A. K.; Grigorenko, A. N.; Novoselov, K. S.; Ferrari, A. C. *ACS Nano* **2010**, *4*, 5617–5626.

(12) Wang, P.; Zhang, W.; Liang, O.; Pantoja, M.; Katzer, J.; Schroeder, T.; Xie, Y.-H. *ACS Nano* **2012**, *6*, 6244–6249.

(13) Gan, X.; Mak, K. F.; Gao, Y.; You, Y.; Hatami, F.; Hone, J. *Nano Lett.* **2012**, DOI: 10.1021–nl302746n.

(14) Kneipp, K.; Wang, Y.; Kneipp, H.; Perelman, L.; Itzkan, I.; Dasari, R.; Feld, M. *Phys. Rev. Lett.* **1997**, *78*, 1667–1670.

(15) Bunch, J. S.; Dunn, M. L. *Solid State Communications* **2012**, *152*, 1359–1364.

(16) Koenig, S. P.; Boddeti, N. G.; Dunn, M. L.; Bunch, J. S. *Nature Nanotechnology* **2011**, *6*, 543–546.

(17) Jiao, X.; Goeckeritz, J.; Blair, S.; Oldham, M. *Plasmonics* **2009**, *4*, 37–50.

(18) Moskovits, M. *Reviews of Modern Physics* **1985**, *57*, 783–826.

(19) Kerker, M.; Wang, D. S.; Chew, H. *Appl Opt* **1980**, *19*, 4159–4174.

(20) Yoon, D.; Moon, H.; Son, Y.-W.; Choi, J. S.; Park, B. H.; Cha, Y. H.; Kim, Y. D.; Cheong, H. *Phys. Rev. B* **2009**, *80*, 125422.

(21) Wang, Y. Y.; Ni, Z. H.; Shen, Z. X.; Wang, H. M.; Wu, Y. H. *Appl. Phys. Lett.* **2008**, *92*, 043121.

(22) Mohamed, M. B.; Volkov, V.; Link, S.; El-Sayed, M. A. *Journal of Photochemistry and Photobiology A: Chemistry* **2000**, *317*, 517–523.

(23) Mohiuddin, T.; Lombardo, A.; Nair, R. R.; Bonetti, A. *Phys. Rev. B* **2009**, *79*, 205433.

(24) Huang, M.; Yan, H.; Heinz, T. F.; Hone, J. *Nano Lett.* **2010**, *10*, 4074–4079.

(25) Tomori, H.; Kanda, A.; Goto, H.; Ootuka, Y.; Tsukagoshi, K.; Moriyama, S.; Watanabe, E.; Tsuya, D. *Applied Physics Express* **2011**, *4*, 5102.

(26) As the $2D'$ mode is an intravalley scattering process, a slight dependence on changes in the electronic due to strain occurs. This effect, however, is already included in the experimental determination of the Grüneisen parameter.

(27) Nye, J. F. *Physical Properties of Crystals: Their Representation by Tensors and Matrices*, first edition ed.; Oxford: At the Clarendon Press, 1957.

(28) Reich, S.; Jantoljak, H.; Thomsen, C. *Phys. Rev. B* **2000**, *61*, 78729.

(29) As the topography indicates that $\varepsilon_y > \varepsilon_x$, we define the shear strain so that it remains positive.

(30) Due to generally low intensities, the line scans were performed using a grating of lower resolution and an larger slit width compared to the spectra shown in Figure 2(a) and (b), which leads to an increase of the FWHM of the G and $2D'$ peaks.

(31) Zabel, J.; Nair, R. R.; Ott, A.; Georgiou, T.; Geim, A. K.; Novoselov, K. S.; Casiraghi, C. *Nano Lett.* **2012**, *12*, 617–621.

(32) Frank, O.; Mohr, M.; Maultzsch, J.; Thomsen, C.; Riaz, I.; Jalil, R.; Novoselov, K. S.; Tsoukleri, G.; Parthenios, J.; Papagelis, K.; Kavan, L.; Galiotis, C. *ACS Nano* **2011**, *5*, 2231–2239.

(33) Yoon, D.; Son, Y.-W.; Cheong, H. *Phys. Rev. Lett.* **2011**, *106*, 155502.

(34) Narula, R.; Bonini, N.; Marzari, N.; Reich, S. *Phys. Rev. B* **2012**, *85*, 115451.

(35) Casiraghi, C.; Hartschuh, A.; Lidorikis, E.; Qian, H.; Harutyunyan, H.; Gokus, T.; Novoselov, K. S.; Ferrari, A. C. *Nano Lett.* **2007**, *7*, 2711–2717.

(36) Narula, R.; Panknin, R.; Reich, S. *Phys. Rev. B* **2010**, *82*, 045418.

(37) Reed, J. C.; Zhu, H.; Zhu, A. Y.; Li, C.; Cubukcu, E. *Nano Lett.* **2012**, *12*, 4090–4094.

Acknowledgement

The authors thank P. Klar, F. Ernst and P. May for fruitful discussions. SH, RN, and SR acknowledge funding by German Research Foundation (DFG via SFB 658, subprojects A6 and B8; DFG via EraNet (Nanospec, 566322)) as well as the ERC (grant number 210642). RFG and SAM acknowledge funding by the Leverhulme Trust (UK) and the UK Engineering and Physical Sciences Research Council (EPSRC). AO, AV and FS acknowledge the Engineering and Physical Science Research Council (EPSRC) UK (grant reference EP/G035954/1).

Supporting Information Available

Fabrication and structural characterization; optical characterization; simulations; AFM data in dimers before and after graphene deposition; microscope images of graphene flake; AFM data and graphene topography on different structure; 2D peak fits for P_X; Raman line scan raw data for 638 nm excitation; laser spot profile; intensity drop for 532 nm excitation.

This material is available free of charge via the Internet at `http://pubs.acs.org/`.

SUPPORTING INFORMATION

Polarized plasmonic enhancement by Au nano structures probed through Raman scattering of suspended graphene

Sebastian Heeg,* Roberto Fernandez-Garcia, Antonios Oikonomou, Fred Schedin, Rohit Narula, Stefan A.Maier, Aravind Vijayaraghavan, and Stephanie Reich

E-mail: sebastian.heeg@physik.fu-berlin.de

*To whom correspondence should be addressed

Contents

Fabrication and structural characterization

Two sets of plasmonic structures which consist of dot patterns with different geometrical shapes and sizes were exposed by electron-beam lithography in a LEO 1530 Gemini FEG SEM and Raith Elphy Plus Lithography System with Laser Interferometer Stage. Metallization was carried out by evaporating 5 nm Cr + 40 nm Au followed by lift-off in an ultrasonic bath. Structural characterization of the nanostructures was done using a Veeco Dimension 3100 AFM and an XL30 Sirion FEI FEG SEM. Graphene flakes were prepared on p-doped Si substrate with 300 nm surface SiO_2 by micromechanical cleavage.[1] The graphene was then accurately transferred on top of plasmonic structures. A polymer was used to coat the graphene flake for supporting it during its transfer on the target substrate using the so called 'wet' transfer method.[2] Structural characterization after graphene transfer was performed using a Park Systems XE 150 AFM.

Optical characterization

Raman spectra were taken using a Horiba XploRA single-grating Raman spectrometer equipped with notch filters for laser rejection and a piezo stage for mapping. Laser excitations of 532 nm and 638 nm and gratings of 600, 1200, and 1800 grooves per mm were employed, with resolutions between $1\,\mathrm{cm}^{-1}$ and $4\,\mathrm{cm}^{-1}$. Typical integration times range between 10 s and 120 s seconds. The spectra were calibrated using a neon lamp. In order to record Raman spectra for different polarizations, the sample was rotated by 90°.

In the darkfield microscopy setup, the sample was illuminated by a polarized white light from a halogen bulb. A 50x, NA 0.55, IR-corrected microscope objective was used to collect the scattered light that is directed to a spectrometer which is equipped with a CCD detector to obtain the spectra in the visible range.

Simulations

For our numerical calculations, Three-dimensional (3D) simulations were performed to calculate the scattering cross sections and the near field enhancement of the coupled nanostructures by using a commercially available finite-difference-timedomain code (Lumerical FDTD). The dielectric functions of Au used in the simulations were extracted from data by Johnson and Christy.[3]

AFM data on structure before and after graphene deposition

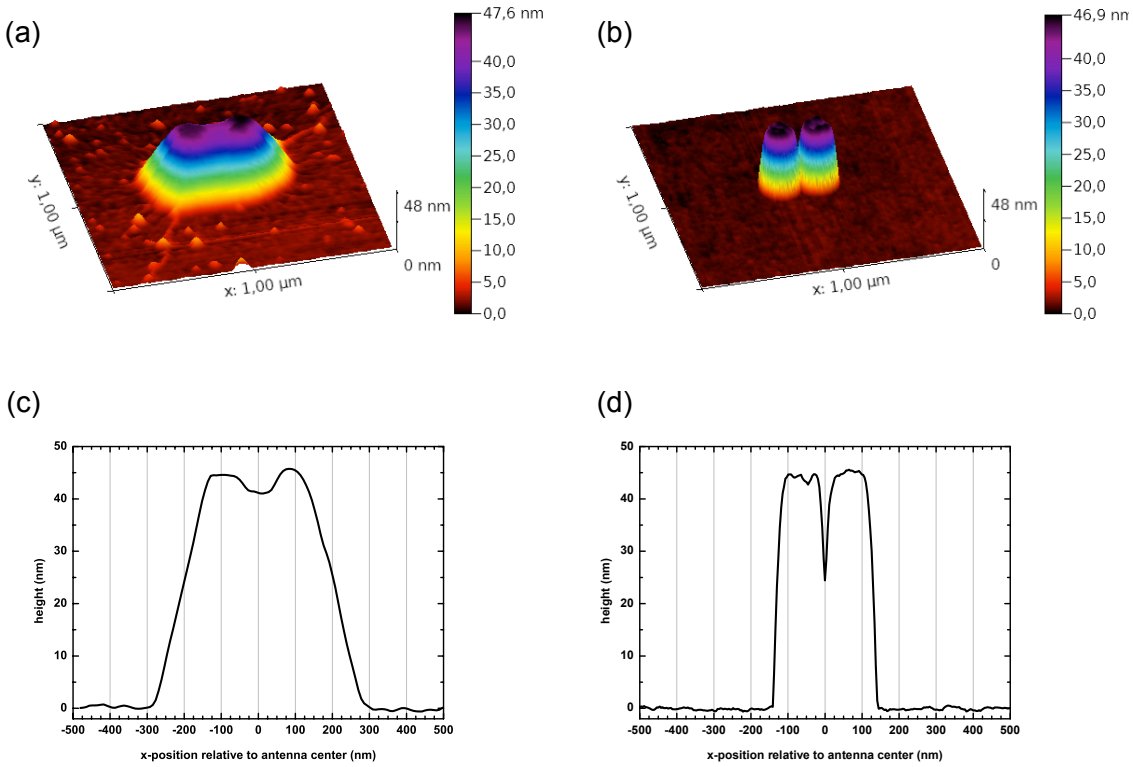

Figure 1: (a) 3D-AFM profile of the structure investigated. In (b) a different structure before graphene deposition is shown. Comparing height profiles across the gap in x-direction before (d) and after graphene deposition (c) confirms that graphene is suspended in the gap and between the edges of the structures and the substrate. While the AFM-data was obtained using different setups - and therefore different tips - the comparison between the height profiles rules out any misinterpretation with respect to the observed topography

Microscope images of graphene flake

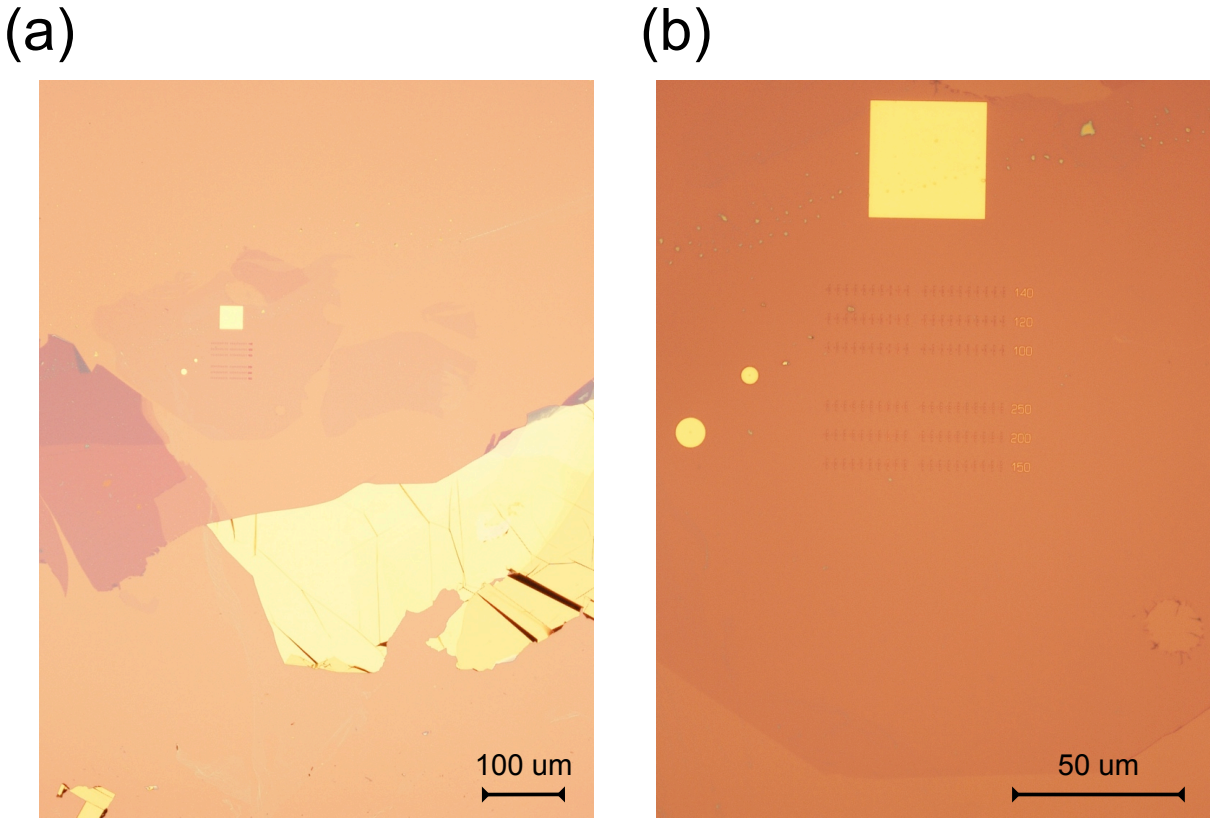

Figure 2: Optical microscope images of the graphene flake deposited on top of the array of double structures after graphene deposition.

AFM data and graphene topograhpy on different structure

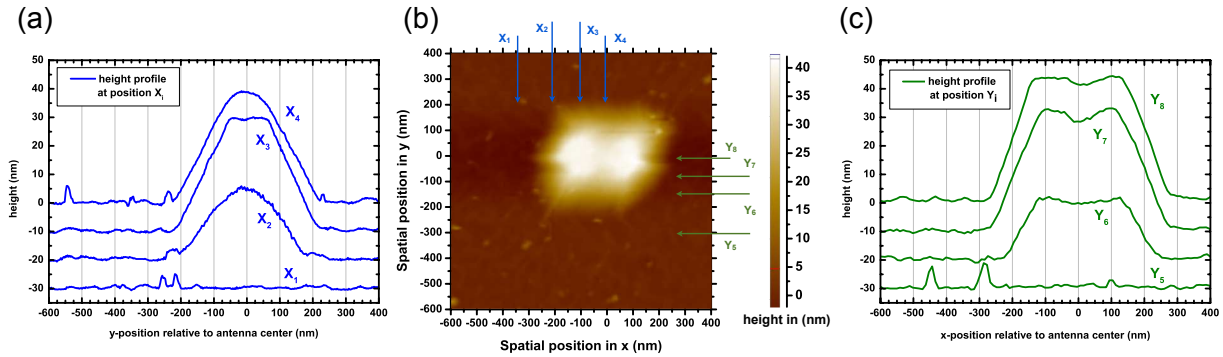

Figure 3: AFM data (b) and corresponding height profiles in for fixed x- (a) and y-values (b) for a double dot structure of 120 nm diameter.

2D peak fits for P_X

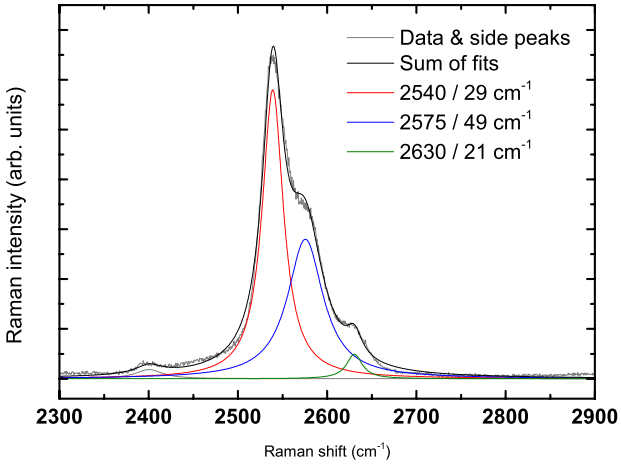

Figure 4: Fits including parameters on the structure, 638 nm excitation and P_X. While the two main components arise from suspended graphene under strain, the minor high frequency component arise from unperturbed graphene which is not subject to plasmonic enhancement.

Raman line scan raw data

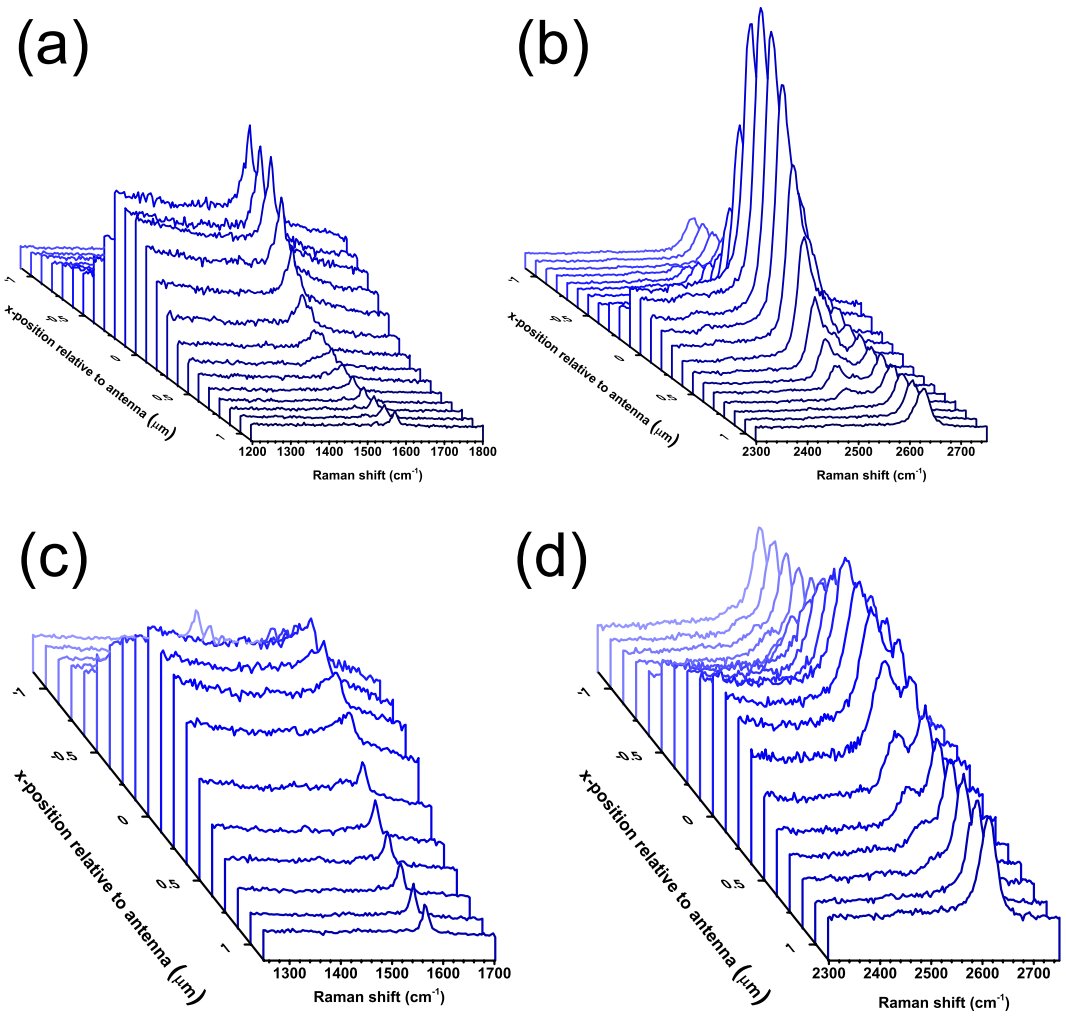

Figure 5: Raman lines scans over the double structure in x-direction showing the evolution of the *G*-peak (a) and 2*D*-peak (b) for P_X and 638 nm excitation. The corresponding line scans for P_Y and shown in (c) and (d).

Laser spot profile

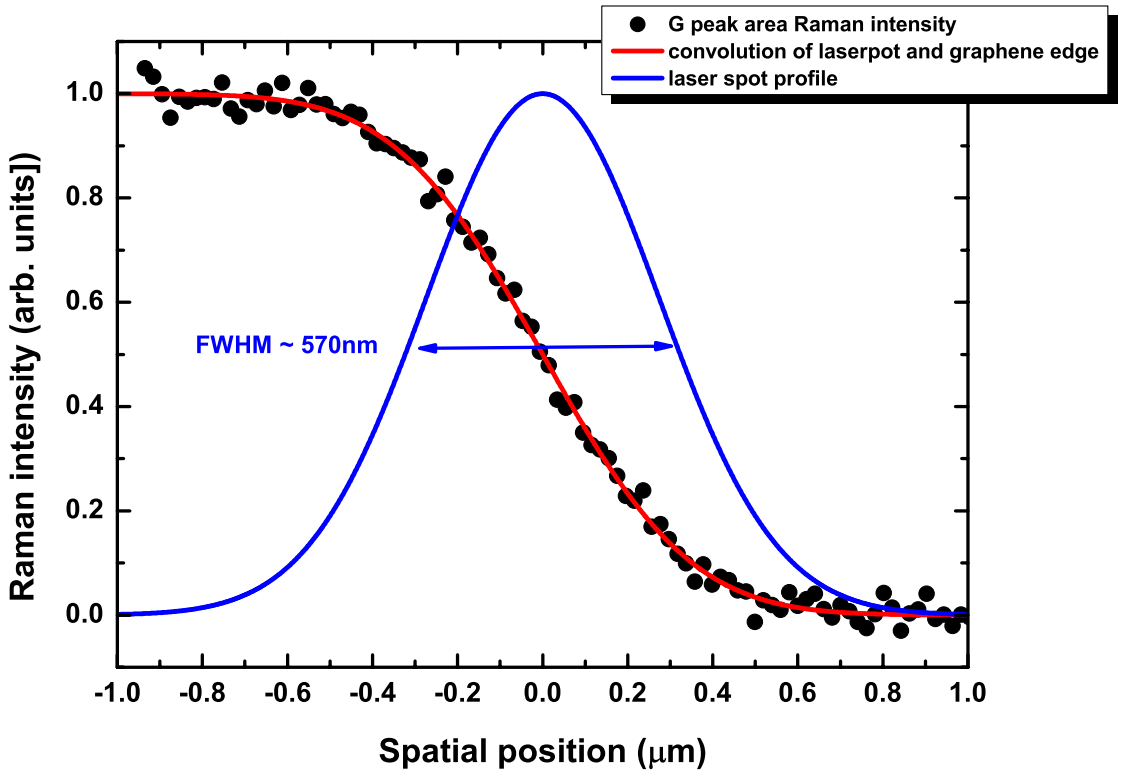

Figure 6: Line scan over a graphene edge for $\lambda = 638\,\text{nm}$ and P_X. The integrated G peak intensity (dots) is fitted by the convolution of a *Heaviside* step function and a Gaussian profile. The resulting Gaussian profile represents the laser spot.

Intensity drop for 532 nm

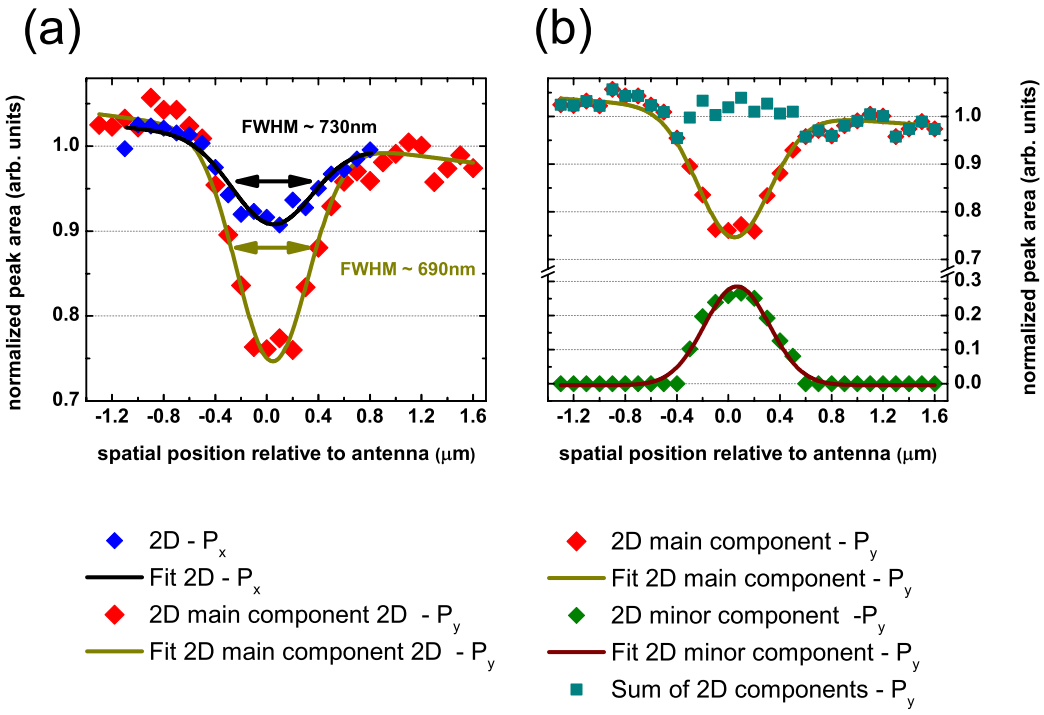

Figure 7: Integrated 2*D* intensities extracted from line scans over the double structure for an excitation of 532 nm. (a) compares the intensity drop on the structure for P_X with corresponding drop of the main 2*D* component for P_Y. (b) shows the intensity profile of the two 2*D* components for P_Y.

Here we depict the variation of the 2*D* integrated intensity along a line scan over the structure for 532 nm excitation and both polarizations. For P_X, the intensity drops $\approx 8\%$ in the structure. We attribute the intensity drop to the lowered Raman intensity observed for graphene placed on top of gold (not shown) as well as the variation of the interference condition for the suspended parts of the graphene sheet. Qualitatively, the width of the intensity drop (730 nm) represents the effect of the sample configuration without plasmonic enhancement. The 2*D* peak for P_Y has to be fitted with two Lorentzian peaks. The intensities are shown in (b). The appearance of a second notable 2*D* component indicates a minor enhancement occurring for P_Y, in agreement with a blue

shifted resonance compared to P_X. This small enhancement compensates for the small intensity drop observed for P_X. The sum of the intensity of the two $2D$ components does not show a drop as for P_X. The width of the intensity drop of the main $2D$ component for P_Y, (690 nm) serves as an indicator of the effect of the structure for P_Y. Combining the line scans for both polarizations allow us to transform the effect of the structures into a spatial profile with a FWHM of 710 ± 10 nm. Note that the width of the laser spot for 532 nm is slightly smaller than for 638 nm. If no enhancement were present for 638 nm, we would therefore expect the effect of the structure to be slightly more extended.

References

1. Novoselov, K. S.; Geim, A. K.; Morozov, S. V.; Jiang, D.; Zhang, Y.; Dubonos, S. V.; Grigorieva, I. V.; Firsov, A. A. Electric field effect in atomically thin carbon films. *Science* **2004**, *306*, 666–669.

2. Reina, A.; Jia, X.; Ho, J.; Nezich, D.; Son, H.; Bulovic, V.; Dresselhaus, M. S.; Kong, J. Large Area, Few-Layer Graphene Films on Arbitrary Substrates by Chemical Vapor Deposition. *Nano Lett.* **2009**, *9*, 30–35.

3. Johnson, P. B.; Christy, R. W. Optical Constants of the Noble Metals. *Phys. Rev. B* **1972**, *6*, 4370–4379.